

# Drop by drop backscattered signal of a 50x50x50m<sup>3</sup> volume: A numerical experiment

Auguste Gires, Ioulia Tchiguirinskaia, D Schertzer

► **To cite this version:**

Auguste Gires, Ioulia Tchiguirinskaia, D Schertzer. Drop by drop backscattered signal of a 50x50x50m<sup>3</sup> volume: A numerical experiment. Atmospheric Research, Elsevier, 2016, 178-179, pp.164 - 174. 10.1016/j.atmosres.2016.03.024 . hal-01673403

**HAL Id: hal-01673403**

**<https://hal-enpc.archives-ouvertes.fr/hal-01673403>**

Submitted on 18 Apr 2019

**HAL** is a multi-disciplinary open access archive for the deposit and dissemination of scientific research documents, whether they are published or not. The documents may come from teaching and research institutions in France or abroad, or from public or private research centers.

L'archive ouverte pluridisciplinaire **HAL**, est destinée au dépôt et à la diffusion de documents scientifiques de niveau recherche, publiés ou non, émanant des établissements d'enseignement et de recherche français ou étrangers, des laboratoires publics ou privés.

1 Drop by drop backscattered signal of a  $50 \times 50 \times 50 \text{ m}^3$  volume: a numerical experiment

2

3 A. Gires<sup>1</sup>, I. Tchinguirinskaia<sup>1</sup>, and D. Schertzer<sup>1</sup>

4 (1) Université Paris-Est, Ecole des Ponts ParisTech, HM&Co, Marne-la-Vallée, France

5 Correspondence to: A. Gires (auguste.gires@enpc.fr)

6

7 Abstract

8 The goal of this paper is to analyse the influence of individual drop positions on backscattered  
9 radar signal. This is achieved through a numerical experiment: a 3D rain drop field generator  
10 is developed and implemented over a volume of  $50 \times 50 \times 50 \text{ m}^3$ , and then the sum of the  
11 electromagnetic waves backscattered by its hydrometeors is computed. Finally the temporal  
12 evolution over 1 second is modelled with simplistic assumptions. For the rainfall generator,  
13 the Liquid Water Content (LWC) distribution is represented with the help of a multiplicative  
14 cascade down to 0.5 m, below which it is considered as homogeneous. Within each  $0.5 \times 0.5$   
15  $\times 0.5 \text{ m}^3$  patch, liquid water is distributed into drops, located randomly uniformly according to  
16 a pre-defined Drop Size Distribution (DSD). Such configuration is compared with the one  
17 consisting of the same drops being uniformly distributed over the entire  $50 \times 50 \times 50 \text{ m}^3$   
18 volume.

19 Due to the fact that the radar wave length is much smaller than the size of a rainfall “patch”, it  
20 appears that, in agreement with the theory, we retrieve an exponential distribution for  
21 potential measures on horizontal reflectivity. Much thinner dispersion is noticed for  
22 differential reflectivity. We show that a simple ballistic assumption for drop velocities does  
23 not enable to reproduce radar observations, and turbulence should be taken into account.  
24 Finally the sensitivity of these outputs to the various model parameters is quantified.

25

26 Keywords:

27 Radar, raindrop, interference, scattering

28

29 1) Introduction

1 Weather radars are the only sensors capable of performing a spatio-temporal measurement of  
2 rainfall fields. It is a remote technique which basically relies on the analysis of the electro-  
3 magnetic field backscattered by hydrometeors in the atmosphere. It means that the quantity  
4 measured by radars is an electric field (or two electric fields when double polarizations are  
5 used), instead of the quantity hydro-meteorologists are interested in, like rain rate (or a Liquid  
6 Water Content, *LWC*). Weather radars suffer from numerous limitations which are due either  
7 to meteorological issues (natural vertical profiles of reflectivity, rainfall changes between the  
8 place of measurement and ground level,) or to the propagation of an electromagnetic wave in  
9 the atmosphere (beam blockage, attenuation, ground echo, anomalous propagation...) (Bringi  
10 and Chandrasekar 2001, Steiner 2005). In this paper we address the specific issue of how the  
11 micro-configuration of drops in position and size affects the large scale scattering properties.  
12 Indeed the electric field measured by radars is the sum of the ones backscattered by individual  
13 drops and can therefore be affected by constructive or destructive interferences leading to  
14 biased rain rate estimates. The study in this paper is focused on the backscattering by  
15 hydrometeors that is a first step towards improved radar measurement.

16 This issue is usually neglected by authors who simply assume a homogenous distribution of  
17 drops within the scanned volume (see Lawson and Uhlenbeck, 1950, for a first description of  
18 this statistical model). Some nevertheless addressed it. For example Jameson and Kostinski  
19 (2010a) analysed the time series of a given range bin with the help of spectral analysis and  
20 found evidence for coherent backscattering. In a refinement of this study, in which they also  
21 analysed the correlations between consecutive radar bins, they confirmed that observations  
22 could not be explained only by noise and associated them with the presence of structures in  
23 the rainfall fields being in resonance with the radar wavelength (Jameson and Kostinski,  
24 2010b). They also noticed that this effect was much more pronounced with snow than with  
25 rainfall and that it increased with radar wavelength (no coherency would be observed if the  
26 radar wavelength tended to 0 mm). Erkelens et al. (2001) explained that many radar  
27 observations can be explained by incoherent hydrometeor scattering and coherent air  
28 scattering (known as Bragg scattering) due to the turbulent fluctuations of the refractive  
29 index. They derived a theoretical expression for coherent scattering by considering the  
30 influence of hydrometeors on the variations of refractive index. The importance of this effect  
31 increases with radar wavelength. Using dual frequency radar measurements and the fact that  
32 the two effects do not have the same dependency on radar wavelength they re-interpreted the  
33 cloud measurements data from Knight and Miller (1998). The effect of the refractive index is

1 not addressed here. Lovejoy et al. (1996) and Schertzer et al. (2012) adopted a different  
2 approach. They modelled sub-radar pixel variability with the help of Universal Multifractal  
3 (Schertzer and Lovejoy 1987, 2011) and derived a theoretical expression linking the actual  
4 radar reflectivity to the theoretical one obtained for incoherent scattering. The underlying idea  
5 being that the clustering of drops will lead to constructive interference.

6 In this paper we adopt an approach different than those previously mentioned, by setting up a  
7 purely numerical experiment to mimic backscattering by hydrometeors located within a  
8 volume of  $50 \times 50 \times 50 \text{ m}^3$ . In order to actually mimic radar measurements, other effects, such  
9 as antenna direction and range patterns, attenuation, propagation effect, or presence of non  
10 clear air along the path the radar wave, would have to be modelled. Some authors, for  
11 example, Capsoni and d'Amico (1998) and later Capsoni et al. (2001) for an extension to  
12 polarimetric quantities, developed radar simulators, but they did not take into account all the  
13 drops due to computation limitations (they used compressed Drop Size Distribution) and also  
14 assumed an homogenous distribution of drops within a radar bin. This was also the case for  
15 Cheong et al. (2008) who used an even smaller amount of hydrometeors per radar bin (few  
16 tens) but simulated time series. Here the contribution of all drops is taken into account,  
17 including their inhomogeneous distribution in space. Other radar simulators were developed  
18 to improve radar rainfall measurements (Anagnostou and Krajewski 1997 or Krajewski et al.  
19 1993 for an earlier version; Doviak and Zrnich 1993) or to produce reflectivity maps from  
20 numerical weather models as a first step toward radar assimilation (Caumont et al. 2006).  
21 These radar simulators rely on the computation of integrals over radar bins and assume a  
22 homogenous distribution of drops, and no coherence effect. Radar data has also been used to  
23 calibrate a 4 level Poisson clustering process to model rainfall fields (Kavvas and Chen,  
24 1989). More recently, this approach of numerical experiment has for example been used in  
25 Merker et al. 2015 to improve radar calibration, but not at the drop scale as done in this paper.

26 In order to achieve our goal of mimicking the scattering of hydrometeors contained within a  
27  $50 \times 50 \times 50 \text{ m}^3$  box we first develop a 3D rain drop field generator (section 2). Then we  
28 compute the electric field measured by the radar as the sum of the electric fields backscattered  
29 by each individual drops and test the influence of the drops' positions (section 3 on  
30 methodology). Finally results for single pulse measurements and successive ones over 1 s are  
31 discussed in section 4.

32

1 2) A large (few tens of meters) scale 3D drop simulator

2 The purpose of this paper is to mimic the scattering of a fixed volume by computing the  
3 electric field backscattered individually by all the hydrometeors it contains. The main  
4 challenge is to generate 3+1 D (3 dimensions in space and 1 dimension in time) rain drop  
5 fields. We aim at simulating during 1 s the signal backscattered by a fixed cubic (i.e. neither  
6 the shape nor the volume of an actual radar bin) volume of size  $50 \times 50 \times 50 \text{ m}^3$ .

7 In order to achieve this, we mainly rely of the findings of Lilley et al. (2006) who analysed  
8 the output of the HYDROP experiment (Desauliner-Soucy et al, 2001) consisting in the  
9 reconstruction of rain drop fields with most of the drops in a  $8 \text{ m}^3$  volume with the help of  
10 stereo-photography; and Gires et al. (2015) who reconstructed vertical 35 m high columns  
11 above a 2D – Video Disdrometer. Their main conclusion was that rain drop related fields  
12 (number, LWC, ...) basically exhibited a scaling behaviour well characterized with the help  
13 of Universal Multifractals (see Schertzer and Lovejoy 2011 for a recent review) down to 0.5  
14 m. Below this scale a homogeneous distribution is found. Based on this a three step process is  
15 designed to generate a 3D rain drop field (see Fig. 1 for an illustration):

16 (i) An average *LWC* is set for the whole  $50 \times 50 \times 50 \text{ m}^3$  volume (it is an input of the model)  
17 and a 3D conservative discrete Universal Multifractal (UM) cascade is implemented to  
18 distribute it over patches of size  $0.5 \times 0.5 \times 0.5 \text{ m}^3$ . Potential anisotropy between horizontal  
19 and vertical directions is not taken into account in this process. Such multiplicative cascade  
20 process is characterized with the help of only two parameters;  $C_1$  the mean intermittency  
21 which quantifies the clustering of the average field ( $C_1 = 0$  for a homogeneous fields), and  $\alpha$   
22 the multifractality index ( $0 \leq \alpha \leq 2$ ) which quantifies how this mean intermittency evolves  
23 when considering field values slightly different from the average one. The greater the values  
24 of UM parameters  $C_1$  and  $\alpha$ , the stronger the extremes. Since the average value of the field is  
25 kept constant, the disparities between the patches will be more pronounced for greater values  
26 of UM parameters.  $C_1$  and  $\alpha$  are inputs of the model.

27 (ii) The second step consists in converting the liquid water within each patch (simply equal to  
28 the  $LWC_{patch}$  in  $\text{g.m}^{-3}$  obtained at the end of the cascade process multiplied by  $0.5 \times 0.5 \times 0.5$   
29  $\text{m}^3$ ) into drops. To achieve this, a discrete Drop Size Distribution is used  $Nb(D_i)$  (the number  
30 of drops of diameter within the class  $D_i$  per unit volume).  $Nb(D_i)$  is decomposed into two  
31 parts:

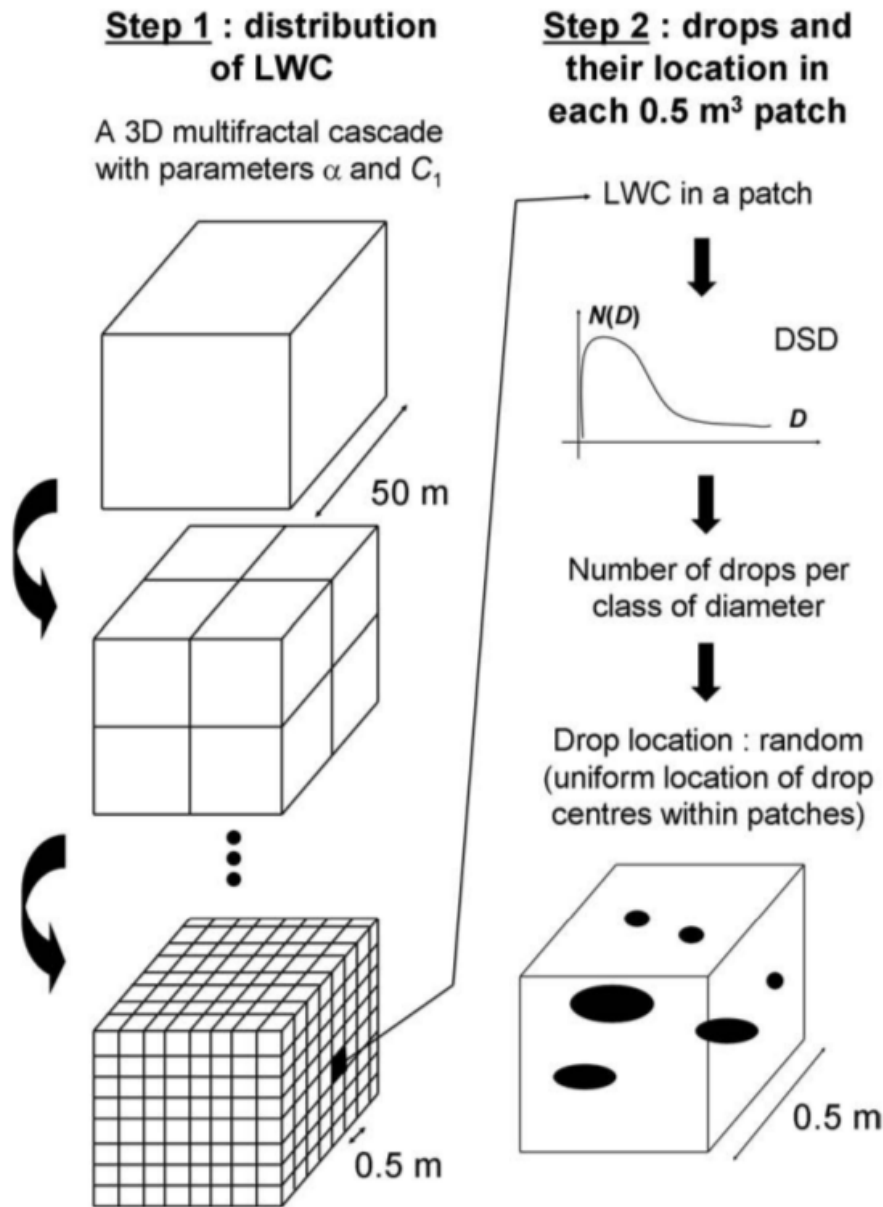
$$1 \quad Nb(D_i) = N_t f(D_i) \quad (1)$$

2 Where  $N_t$  is the number per unit volume and  $f(D_i)$  is simply the proportion of drops within  
 3 a given class ( $\sum_{class} f(D_i) = 1$ ).  $f(D_i)$  is an input of the model. For each patch only  $N_{t,patch}$  has  
 4 to be evaluated. Finally the number of drops of a given class within a given patch is equal to  
 5  $N_{t,patch} f(D_i)$ . In practice the nearest integer is used.  $N_{t,patch}$  is obtained by ensuring that the  
 6 sum of the mass of all the drops equals the liquid water content of the patch:

$$7 \quad LWC_{patch} V_{patch} = \rho_{wat} \frac{4}{3} \frac{1}{10^9} \pi N_{t,patch} \sum_i \left( \frac{D_i}{2} \right)^3 f(D_i) \quad (2)$$

8 With  $D_i$  in mm,  $\rho_{wat}$  the water volumic mass in  $\text{g.m}^{-3}$ ,  $V_{patch}$  in  $\text{m}^3$  and  $LWC_{patch}$  in  $\text{g.m}^{-3}$  and  
 9  $D_i$  in mm.

10 (iii) The last step consists in affecting a position to the drop centre. It is done with a simple  
 11 random uniform law for all three directions within the patch.



1  
2 Figure 1. Illustration of the process designed to generate synthetic 3D rain drop fields

3  
4 In section 4.3, we need to consider the temporal evolution of the drops over 1 s, i.e. simulate  
5 their movement. To achieve this, the following steps are implemented: (i) a larger volume is  
6 modelled (100 m in height) (ii) a velocity  $\underline{v}$  is affected to each drop and used to locate them  
7 over successive time steps. Two velocities are tested:

- 8 - A purely vertical (along the vertical axis, characterized by a unit vector  $\underline{e}_z$ ) ballistic one  
9  $\underline{v}_{bal}$ , where a terminal fall velocity depending on the equi-volume diameter is used. The  
10 relation of Lhermitte (1988) is used:

$$1 \quad \underline{v}_{bal}(D) = v_{bal} \underline{e}_z = 9.25 * (1 - \exp(-68002D^2 - 488D)) \underline{e}_z \quad (3)$$

2 Where  $v_{bal}$  is in  $\text{m.s}^{-1}$  and  $D$  in mm. This standard assumption for drop velocity is done here,  
3 although some recent works showed that there were some discrepancies between “theoretical”  
4 fall velocity and actual fall velocity in real condition due notably to the constantly alive  
5 collision - break-up – relaxation process (Montero-Martinez et al. 2009). Deviations seem to  
6 be more pronounced for convective storms than stratiform ones (Niu et al. 2010, Thurai et al.  
7 2013). It would be interesting to investigate the effect of this issue on radar measurement with  
8 a numerical simulator in future work.

9 - A turbulent one  $\underline{v}_{turb}$ , which takes into account a potential horizontal variability

$$10 \quad \underline{v}_{turb} = v_{bal} \underline{e}_z + v_{trub,max} (U \underline{e}_x + V \underline{e}_y) \quad (4)$$

11 where  $U$  and  $V$  are i.i.d. uniform random variables between -0.5 and 0.5.  $v_{trub,max}$  is a  
12 parameter set by the user defining the range of values over which the turbulent velocity can  
13 vary. Values equal to 1, 2, and 4  $\text{m.s}^{-1}$  were tested. Adding a constant horizontal average wind  
14 for all drops did not affect the results that will be discussed in section 4.3, hence it is not done.  
15 The most relevant point is the differences of velocities between drops. The authors are aware  
16 that this is a very simplistic model that should be refined for further quantitative analysis but  
17 is sufficient for the illustrative purpose of this section.

18 Multifractal analysis were first carried out on the simulated LWC fields and then on the  
19 reconstructed (simply adding the contribution of each drop) LWC fields obtained after a 1s  
20 movement by a turbulent velocity to check whether the scaling properties of spatial clustering  
21 are preserved. Obviously input UM parameters are retrieved at the beginning of the process.  
22 For the reconstructed fields, the quality of the scaling decreases and UM parameters are  
23 slightly altered (a decrease for both is noted, more pronounced for  $C_1$  and larger initial  
24 values), but the overall properties are kept.

### 25 3) Methods

26 Radars basically measure the intensity of the electric field backscattered by the hydrometeors  
27 located within the scanned volume. More precisely let us consider a radar located at  $(-r,0,0)$  in  
28 a Cartesian coordinate system that transmits a horizontally polarized wave  $E_h^{inc}$  with a wave  
29 length  $\lambda$ . See Fig. 2 for an illustration of the simulated configuration. The distance  $r$  between  
30 the radar transmitting the wave and the fixed volume whose backscattering is computed was



1 set to 15 km in this paper. A wave length equal to 33.3 mm corresponding to X-band is used  
 2 in this paper and similar results are found for C and S band. The electric field  
 3  $E_{h,drop}^{sca}$  backscattered by a drop located at the position  $(x,y,z)$  is equal to:

$$4 \quad E_{h,drop}^{sca} \approx S_{hh,drop} e^{-i\phi_{tot,drop}} \quad (5)$$

5 Where:

6 -  $\approx$  indicates proportionality; pre-factors, being considered as identical for all the drops  
 7 located within the scanned volume, are neglected in this study. It means that all propagation  
 8 effects (attenuation and phase shift of the horizontal and vertical components) along the path  
 9 between the radar and the fixed volume containing the scattering hydrometeors are not  
 10 addressed in this paper. Future works will include them, notably to take into account the  
 11 variability of LWC at small spatio-temporal scales. Note that weighting functions to model  
 12 antenna and pulse beamwidth are not used in this paper which focuses on the scattering by  
 13 hydrometeors. Eq. 5 means that only mono-scattering is considered in this study (the order of  
 14 magnitude of the maximum drop concentration is  $10^3 \text{ m}^{-3}$  here), and potential effects of  
 15 multiple scattering, which tend to increase radar reflectivity (Kobayashi et al. 2005, 2007a,  
 16 2007b), are not taken into account.

17 -  $\phi_{tot}$  is the total phase shift due the two way path between the radar and the drop. We have

$$18 \quad \phi_{tot} = \frac{2\pi\delta}{\lambda} \quad (6)$$

19 With

$$20 \quad \delta = 2\sqrt{(x+r)^2 + y^2 + z^2} \quad (7)$$

21 being the optical path

22 -  $S_{hh}$  is the complex scattering coefficient, computed for an angle corresponding to  
 23 backscattering. This complex number was estimated for each scatterer (a drop) using the  
 24 Python PyTMatrix library (Leinonen 2014) which relies on the T-Matrix code by Mishchenko  
 25 et al. (1996). In order to carry out the computations, the following assumptions were made: (i)  
 26 Oblate spheroids are used to model drop shapes. The axis ratio is determined from the drop's  
 27 volume (through its equivolume sphere diameter) with the help of the relation described in  
 28 Battaglia et al. 2010. Neither the flattening of drops at the bottom, nor their oscillations  
 29 (Thurai et al. 2005, 2009, Okamura 2010) are taken into account. Additional details on the

1 computation of scattering properties of rain drops can be found in the recent review by  
 2 Okamura and Oguchi (2010) and references therein. (ii) The unknown orientation of the  
 3 drops, which is modelled through the canting angle between the symmetry axis along the  
 4 short direction of the drop and the local zenith (Oguchi 1977, Okamura and Oguchi 2010), is  
 5 taken into account by considering a value of  $S_{hh}$  averaged over a distribution of canting  
 6 angles. The one used here is the same as in Leinonen (2012); i.e. a normal distribution with  
 7 mean and standard deviation respectively equal to  $0^\circ$  and  $7^\circ$ , in agreement with the findings of  
 8 Bringi et al. 2008 on artificial rain measurement. Experiments with a video precipitation  
 9 sensor showed that the distribution in actual rainfall condition could be wider (mean and  
 10 standard deviation respectively equal to  $2.1^\circ$  and  $11^\circ$ ), and attributed these discrepancies to  
 11 the wind (Liu et al. 2014). (iii) Computations are carried out at a temperature of  $20^\circ\text{C}$  (the  
 12 complex refractive index of water is then equal to  $8.208+1.886i$ ).

13 The electric field measured by the radar is computed as the sum of the ones backscattered by  
 14 each drop (typically few hundred millions in our simulations):

$$15 \quad E_{h,radar} = \sum_{drops} E_{h,drop}^{sca} \approx \sum_{drops} S_{hh,drop} e^{-i\phi_{tot,drop}} \quad (8)$$

16 Which yields the observed intensity

$$17 \quad I_{h,radar} = |E_{h,radar}|^2 \approx \left| \sum_{drops} S_{hh,drop} e^{-i\phi_{tot,drop}} \right|^2 \quad (9)$$

18 Finally this quantity is compared with the simple sum of the backscattering coefficients

$$19 \quad I_{h,simple} \approx \sum_{drops} |S_{hh,drop}|^2 \quad (10)$$

20 which corresponds to what would be observed if there was no constructive (or destructive)  
 21 interferences between the fields backscattered by each drop (homogeneous distribution of the  
 22 drop centres).

23 Similar computations are carried out for the wave transmitted and received with a vertical  
 24 polarization (replacing “h” by “v” in the notations), and the ratio between the intensities  
 25 measured for both polarisations is estimated (a pseudo radar differential reflectivity):

$$26 \quad I_{hv,radar} = \frac{I_{h,radar}}{I_{v,radar}} \quad (11)$$

1 In order to study the influence of constructive (or destructive) interferences due to the drops'  
2 locations, for each realisation of *LWC* 3D distribution, 100 realisations of drops' positions  
3 within its patch are generated. For each realisation the radar intensity at vertical and  
4 horizontal polarization is computed, leading to an ensemble of 100 samples for each radar  
5 quantity. The exceedance probability distribution, denoted *Pr*, is finally estimated by sorting  
6 the ensemble of values in increasing order and dividing the rank by the total number of  
7 samples. Finally, for each sample, another ensemble obtained by locating randomly  
8 homogeneously the same drops not only within its own patch but within the whole 50 x 50 x  
9 50 m<sup>3</sup> volume is generated. An exceedance probability distribution is computed similarly for  
10 this second ensemble. This enables to study the potential effect of drop clustering (down only  
11 to the patch scale of 0.5 m) on the computed probability distribution.

12

13 The standard set of parameters used in this paper is  $C_1 = 0.2$ ,  $\alpha = 1.8$ ,  $\langle LWC \rangle = 2 \text{ g.m}^{-3}$ , DSD  
14 type 1 (Fig. 3), elevation angle  $\theta = 0^\circ$  (Fig. 2). The sensitivity of the model to its various  
15 parameters is tested by successively varying only one of parameters, while keeping the others  
16 constant:

17 - Influence of UM parameters  $C_1$  and  $\alpha$ :  $C_1$  equal to 0.05, 0.2, and 0.5; and  $\alpha$  equal to 1.8, 1.2,  
18 and 0.6 is tested. This range of parameter values is somewhat typical among empirical  
19 estimates reported for the radar rainfall fields (e.g., Gires et al. 2011, Tchiguirinskaia et al,  
20 2012, Verrier et al. 2010 and 2011). However, it remains larger than the one observed on 3D  
21 fields (Lilley et al. 2006; Gires et al. 2015) for which  $C_1$  and  $\alpha$  estimates are respectively in  
22 the lower and upper bound of the interval studied here. In this paper we keep the wider range  
23 of observed parameters to test in a more general way the influence of UM parameters.

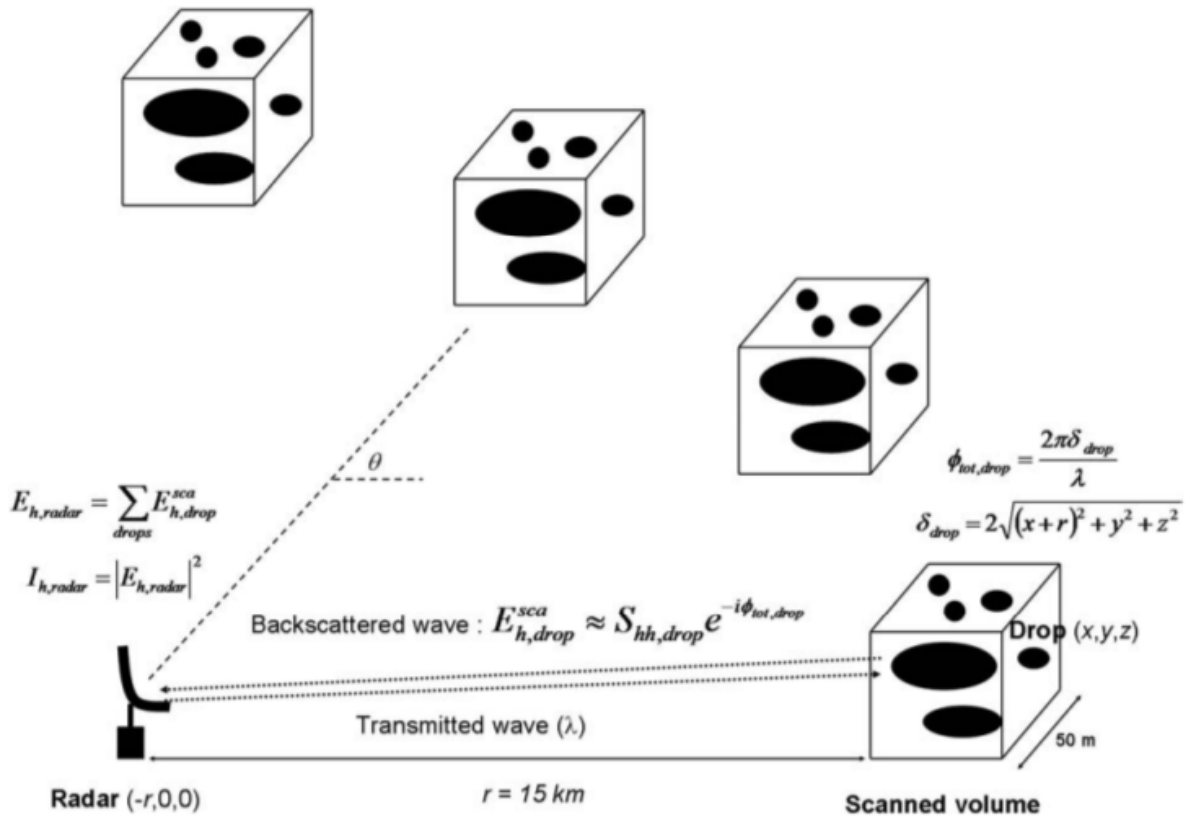
24 - Influence of  $\langle LWC \rangle$ :  $\langle LWC \rangle$  equal to 1, 2, 4, 7 g.m<sup>-3</sup> is tested. This range of values is on  
25 the upper bound of standard observed ones (for example Leinonen et al. 2012 observed LWC  
26 in range 0.01-4 g.m<sup>-3</sup>), because we wanted here to test extreme situations for which radar  
27 rainfall estimates are more sensitive.

28 - Influence of DSD type: two DSDs are tested and the normalized histograms according to the  
29 diameter class are displayed in Fig. 3. They correspond to the ones obtained with the help of a  
30 2D-video disdrometer for two different minutes of an event studied in Gires et al. (2015).  
31 There are more drops with a larger diameter for the second type. It means that for a given

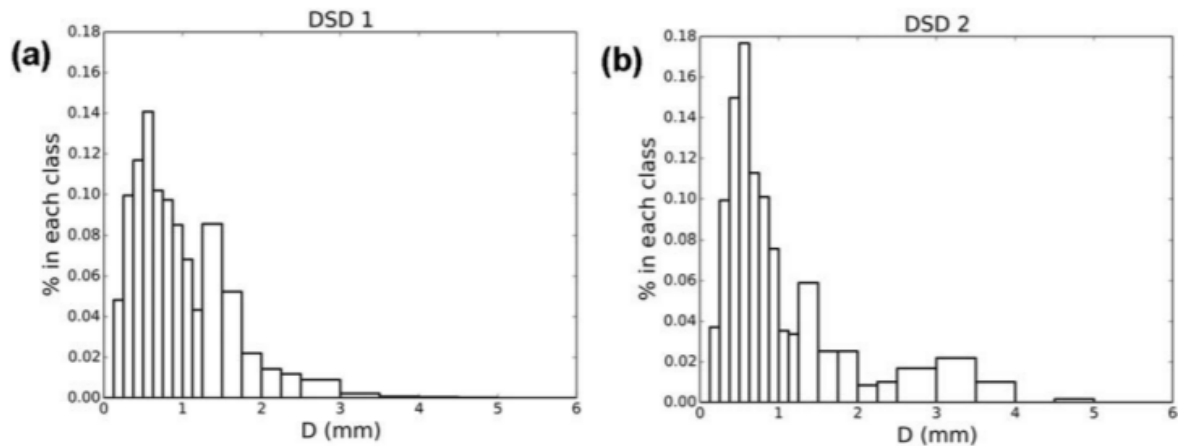
1 average LWC over the studied volume, there are more large drops for the DSD type 2. Both  
 2 DSDs are likely to lack small drops given the low sensitivity of disdrometer measurements to  
 3 small drops. However this should not be a significant issue given that backscattered intensity  
 4 basically behaves as a power 6 of the diameter, which limits the influence of small drops.  
 5 Although they are rather similar, the two DSDs yield significant differences in the  
 6 backscattered signal. Hence it suggests that they are sufficiently different to illustrate the  
 7 point that it is a crucial parameter that should be studied in more details in future work,  
 8 including taking into account its spatial variability.

9 - Influence of the location of the scanned volume with regards to the radar: elevation angles  $\theta$   
 10 equal to 0, 10, 20, 30, 40, 50, 60, 70, 80, 90° (for horizontally to vertically pointing radars)  
 11 are tested. Fig. 2 illustrates the definition of  $\theta$ .

12 For actual rainfall field the model parameters are not independent, and some correlations are  
 13 noted (ex: between the *DSD* and the *LWC*). It means that if the purpose of the sensitivity  
 14 analysis was to quantify measured uncertainties, there would have to be some correlation  
 15 between the parameter changes to explore realistic ranges of possible values. In this first  
 16 study we simply want to test their influence on the outputs, so they are modified  
 17 independently from a standard situation.



1 Figure 2. Illustration of the configuration tested for simulating radar observations of a 50 x 50  
2 x 50 m<sup>3</sup> scanned volume.



4 Figure 3. Histograms (% of drops according to class of diameters) for the two DSD types used  
5 in this paper.

6

#### 7 4) Results and discussion

8 Before discussing the results, it should be mentioned that there is no data available at drop  
9 scale on such a large volume to properly validate the model developed here, which by the way  
10 is also the case for more homogeneous models commonly used in other works. Nevertheless it  
11 is in agreement with some prior results (based on imperfect data, Gires et al. 2015, Lilley et  
12 al. 2006) hinting at scaling properties down to 0.5 m. Further investigations involving both  
13 instrumentations and modelling developments will be needed to improve it as well as to  
14 validate it.

#### 15 4.1) Horizontal reflectivity

16 In this section we only consider the backscattered intensity measured horizontally by a radar  
17 transmitting a horizontal wave. Figure 4.a displays the exceedance probability distribution for  
18 an ensemble obtained from a realisation of *LWC* 3D distribution with  $C_1 = 0.2$ ,  $\alpha = 1.8$   
19 ( $\langle LWC \rangle = 2 \text{ g}\cdot\text{m}^{-3}$ , DSD type 1, elevation angle  $\theta = 0^\circ$ ). The curve corresponding to the  
20 drops' positions affected within their patch is in red whereas the one with the drops' positions  
21 affected within the whole volume is in blue. The green vertical line corresponds to the values  
22 obtained with the simple sum (Eq. 10), which is the same for all the samples given that the  
23 same drops with different locations are considered.

1 The first striking feature is that the two curves are very similar. It means that affecting the  
2 positions of the drops within a patch or within the whole volume does not change the range of  
3 explored values due the constructive or destructive interferences between the electric fields  
4 backscattered by each drop. In other words the clustering of drops does not yield additional  
5 constructive interferences. This finding is in apparent contradiction with the ones of Lovejoy  
6 et al. (1996) and Schertzer et al. (2012). It is actually simply due to the fact that in the specific  
7 model implemented here the clustering of drops stops at 0.5 m which is much greater than the  
8 radar wave length (few cm for radar wavelength), which was not the case in the previously  
9 mentioned paper. This decorrelation between drops and atmospheric turbulence, set here at  
10 0.5 m, is likely to occur at much smaller scale in clouds where drops / droplets are actually  
11 smaller and therefore more sensitive to wind effects (see Lilley et al. 2006 and Gires et al.  
12 2015 for a discussion on this point; or Schmitt et al. 1998 or de Montera et al, 2010 on the  
13 passive scalar like behaviour on rain drops and the coupling with turbulence), meaning that a  
14 different model should be used to study cloud radar observations (Erkelens et al., 2001). To  
15 clarify this point a closer look at Eq. 6 indicates that the influence of the drops' locations on  
16 the backscattered wave is limited to the decimal part of the ratio between the optical path and  
17 radar wave length  $\frac{\delta}{\lambda}$  (the integer part does not need to be considered given that  $e^{2i\pi N} = 1$ ). If  
18 the patch size is much larger than  $\lambda$ , then this ratio will be homogeneously distributed and  
19 drop clustering does not affect the results. It also means that if some rainfall structures are in  
20 resonance with the radar wavelength then some constructive interferences could be observed.  
21 This effect is discussed in Jameson and Kostinski (2010), and not observed with the  
22 developed model.

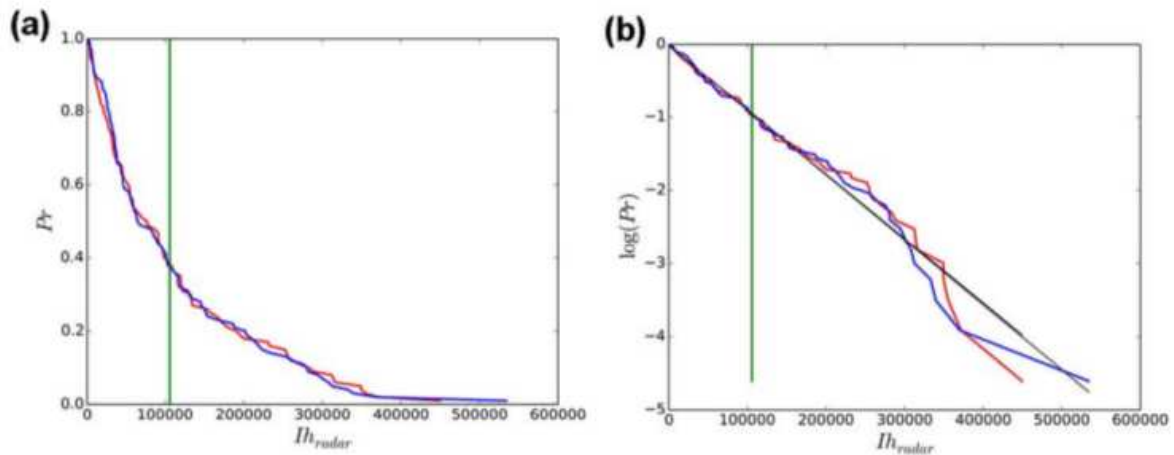
23 The distribution of measured intensity according to the sample of drop locations is skewed  
24 and covers a wide range of possible values. It can be shown theoretically that if drop centres  
25 are homogeneously (uniformly) distributed, the distribution actually follows an exponential  
26 law. The proof, which relies on the central limit theorem, can be found in Lovejoy and  
27 Schertzer (1990). As a consequence one expects:

$$28 \quad \Pr(I_{h,radar} | I_{h,simple}) = \frac{1}{I_{h,simple}} e^{-I_{h,radar} / I_{h,simple}} \quad (12)$$

29 In order to confirm this  $\log(\Pr)$  vs.  $I_{h,radar}$  is plotted in Fig. 4.b for the same ensembles as in  
30 Fig. 4.a. The expected straight lines are retrieved. Linear regressions implemented on the

1 whole ensemble yield inverses of the slopes equal to 113730 and 112812 for respectively the  
 2 ensemble with and without clustering (coefficient of determination greater than 0.98). These  
 3 values are very similar and also close (7% or less) to both  $I_{h,simple}$  (105688) and the mean of  
 4 the ensemble (107583) to which they should be equal for an exponential distribution. Similar  
 5 results are found for the other generated ensembles of this paper.

6



7

8 Figure 4. (a) Exceedance probability distribution  $Pr$  in the ensemble of radar observations  
 9  $I_{h,radar}$  for a given  $LWC$  3D distribution; (red) drops location with clustering down to 0.5 m.  
 10 (blue) drop locations without clustering (b) Same as in (a) expect that  $\log(Pr)$  is plotted  
 11 instead of  $Pr$ .

12

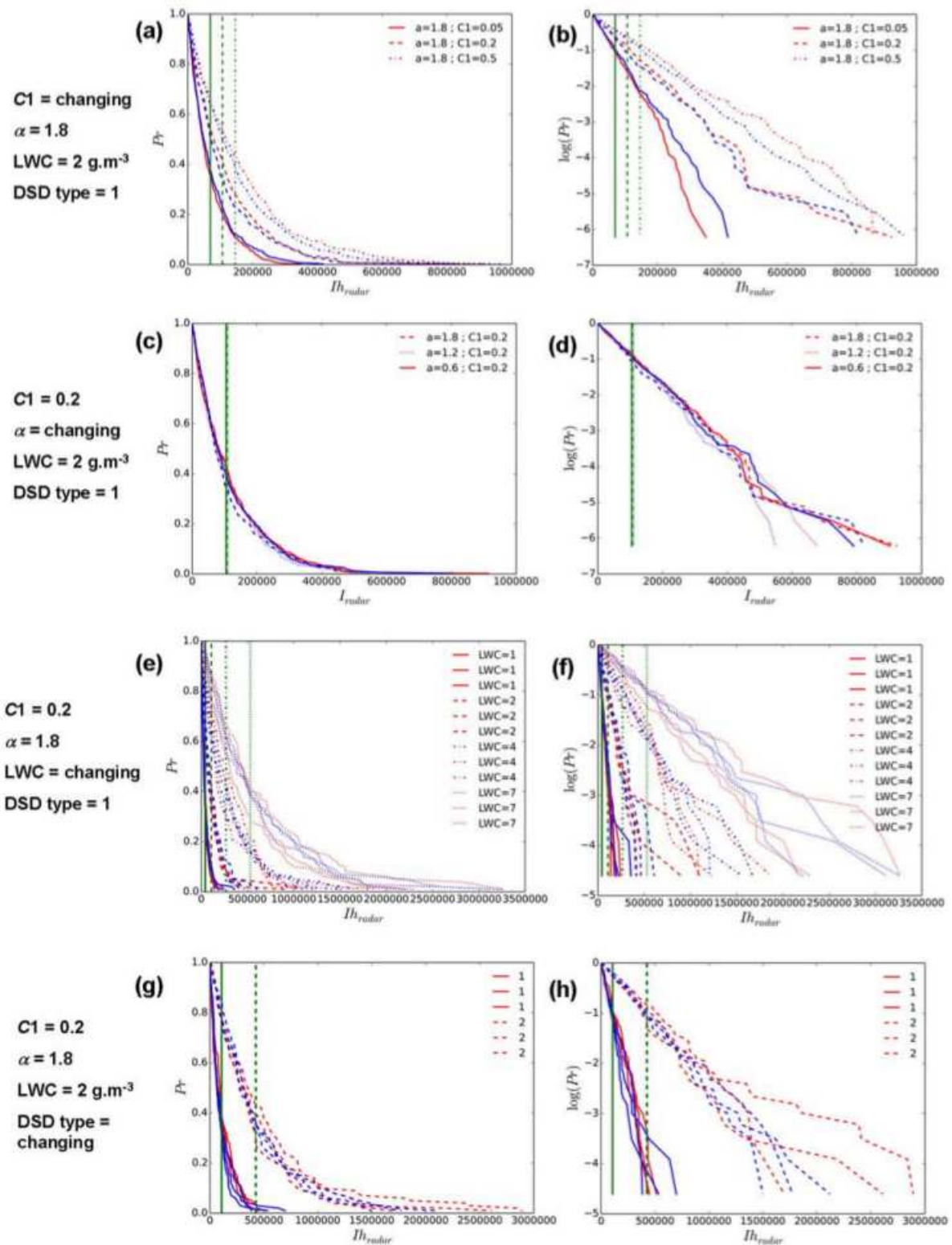
13 Then the influence of the various parameters of the model is analysed, beginning with UM  
 14 parameters. Figure 5.a and b (c and d) display respectively the exceedance probability (or its  
 15 log) vs. the radar intensity for various values of  $C_1$  ( $\alpha$ ), keeping all the others constant. As in  
 16 Fig. 4 the red curves are obtained with clustering (down to 0.5 m) while the blue ones are  
 17 obtained without clustering. Each curve is actually an average obtained with 3 ensembles of  
 18 100 samples obtained from a given  $LWC$  3D distribution. This was done to highlight more  
 19 clearly the differences found for the various UM parameters which were less visible than  
 20 those for the other parameters. The same qualitative results, i.e. an exponential distribution of  
 21 the possible values according to the drop position and no influence of the drop clustering  
 22 (which stops at 0.5 m), are observed for all the parameter sets. Quantitatively it appears that  
 23 the retrieved radar intensities increase with  $C_1$ . This effect is somehow an artefact of the

1 model. When  $C_1$  increases the variability / extremes in the *LWC* 3D distribution is stronger,  
2 meaning the some patches will have much greater values since the average *LWC* remains  
3 constant. These greater values in some patches mean that more large drops will be located in  
4 it. Indeed when the liquid volume of each patch is converted into drops using the DSD, the  
5 nearest integer is used as the number of drops of a given class. It means that greater quantities  
6 of water enable to explore more the tail of the DSD, which corresponds to the drops  
7 backscattering more significantly radar waves. Histograms (not shown here) of drops per  
8 class confirm this interpretation. Given that the range of values for  $C_1$  explored in the  
9 sensitivity analysis is wider than expected from available observations for rainfall (see section  
10 3), this effect is likely to have less influence on actual measurements than noted here. No  
11 influence of  $\alpha$  is observed.

12 Figure 5.e and f display the same curves as in Fig. 5.a and b but for varying average *LWC*.  
13 The only difference is that the curves obtained for each ensemble of 100 samples of drop  
14 positions for a given *LWC* 3D distribution are plotted individually and not on average. The  
15 results simply confirm expectations; i.e. same qualitative results as before and the retrieved  
16 radar intensity obviously increases with greater values of *LWC*. The curves associated with a  
17 given value of average *LWC* are clearly distinguishable from the ones for another value.

18 Figure 6.g and h are the same ones but for the two DSD types, with again the same qualitative  
19 results. Quantitatively as expected all parameters being constant the DSD with heavier tail  
20 (DSD 2) yields greater values of radar intensities since it basically depends on the drops'  
21 diameters to the power 6. Given the strength of this effect especially for DSD not so  
22 significantly different, it would be important to analyse in future works the influence of the  
23 strong hypothesis of homogeneous DSD over the scanned volume. Indeed spatial and  
24 temporal variations in DSD (Schleiss and Smith, 2015) could yield different results. This will  
25 be studied in future investigations.





1  
 2 Figure 5. Influence of the various parameters of the model on the retrieved radar intensities.  
 3 (left) Exceedance probability distribution  $Pr$  in the ensemble of radar observations  $I_{h,radar}$  for  
 4 a given  $LWC$  3D distribution; (right) same as in (left) but plotting  $\log(Pr)$  instead of  $Pr$ . (red)  
 5 drops location with clustering down to 0.5 m. (blue) drop locations without clustering.

1

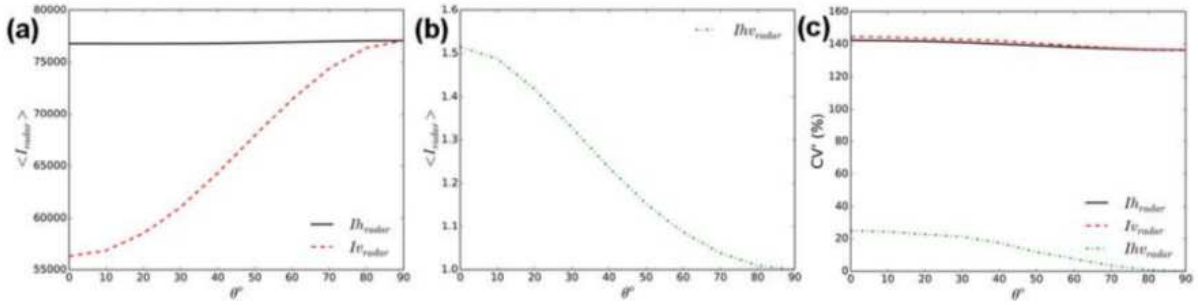
## 2 4.2) Differential reflectivity

3 In this section we analyse not only  $I_{h,radar}$  but also  $I_{v,radar}$  and  $I_{hv,radar}$ , the ratio between the  
4 two. We also consider elevation angles  $\theta$  ranging from 0 to 90°. As commonly done in this  
5 paper, for a given parameter set, an ensemble of 100 samples corresponding to different  
6 drops' positions is generated (either considering clustering down to 0.5 m or not). Here the  
7 standard configuration is used, only  $\theta$  varies. Figure 6.a and b. display the mean among the  
8 ensemble of values for respectively  $I_{h,radar}$  and  $I_{v,radar}$ , when clustering is considered (very  
9 similar results are found without clustering), as a function of  $\theta$ . As expected the differences  
10 between the intensity between the two polarizations is maximum for  $\theta = 0^\circ$  and null for  
11  $\theta = 90^\circ$  (an oblate spheroid seen from below “looks like” a circle). The maximum ratio  
12 obtained between the two is equal to 1.5.

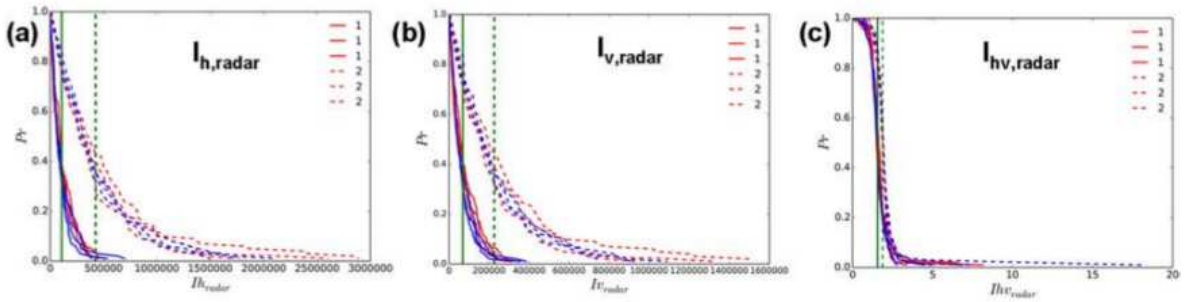
13 The relevant feature is visible in Figure 6.c which displays a pseudo coefficient of variation  
14 ( $CV'$ ) within the ensemble for each angle.  $CV'$  is defined as the difference between the 90%  
15 and 10% quantile divided by twice the mean. It is expressed in %. This pseudo coefficient of  
16 variation is used rather than the standard one because the underlying probability distributions  
17 are skewed. It appears that  $CV'$  is very close for both  $I_{h,radar}$  and  $I_{v,radar}$ , and tends to very  
18 slightly decrease with greater  $\theta$ . The values are also much greater than the ones found for  
19  $I_{hv,radar}$  (140% vs. 25%), which means that the dispersion within the ensemble is much  
20 smaller for  $I_{hv,radar}$ . This quantity is therefore less sensitive to individual drop positions and its  
21 estimates more robust. This is due to the fact that the constructive (or destructive)  
22 interferences between the electric field backscattered at each polarization by drops are  
23 correlated; i.e. to simplify  $I_{h,radar}$  and  $I_{v,radar}$  are affected by the same kind of interferences.

24 In order to have a closer look at the obtained distributions, Fig. 7 displays the exceedance  
25 probability as a function of  $I_{h,radar}$  (Fig. 7.a),  $I_{v,radar}$  (Fig. 7.b) and  $I_{hv,radar}$  (Fig. 7.c). They are  
26 the same curves as in Fig. 4 and 5 right columns. They are plotted for the two DSD types,  
27 with 3 ensembles for each DSD type (i.e. 3 realisations of LWC 3D distribution are tested).  
28 The behaviour observed for the vertical polarization output  $I_{v,radar}$  is very similar to the one  
29 found for  $I_{h,radar}$  which has been discussed in the previous section (exponential distribution,

1 simply with lower values, Fig. 7.b). On the contrary as hinted with the analysis of  $CV'$ , the  
 2 distribution of  $I_{hv,radar}$  exhibits a completely different shape with much less dispersion (Fig.  
 3 7.c). It is neither an exponential nor a Gaussian distribution.



4  
 5 Figure 6.  $\langle I_{h,radar} \rangle$  and  $\langle I_{v,radar} \rangle$  (a) and  $\langle I_{hv,radar} \rangle$  (b) as a function of the elevation angle  $\theta$ . (c)  
 6  $CV'$  within each ensemble of simulated  $I_{h,radar}$ ,  $I_{v,radar}$  and  $I_{hv,radar}$  as a function of the  
 7 elevation angle  $\theta$ .



8  
 9 Figure 7. Exceedance probability distribution  $Pr$  in the ensemble of radar observations for  
 10  $I_{h,radar}$  (a),  $I_{v,radar}$  (b) and  $I_{hv,radar}$  (c). For each DSD type (1 or 2), the results corresponding to  
 11 three ensembles, each obtained for a realisation of  $LWC$  3D distribution, are displayed.

12

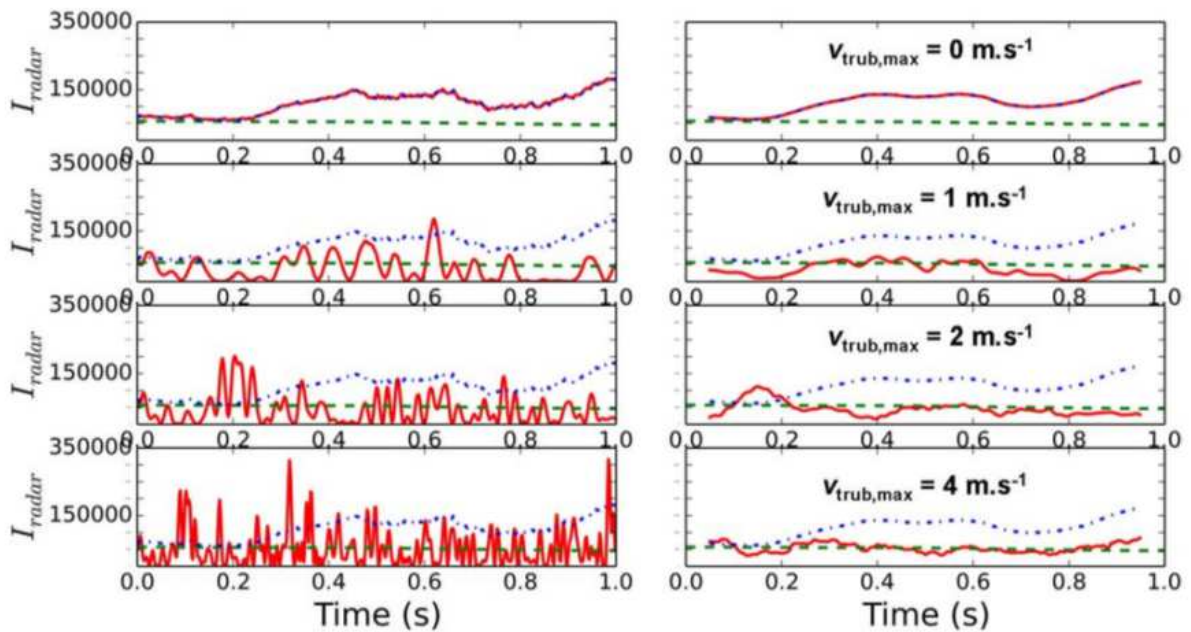
### 13 4.3) Consequences on radar remote sensing

14 In this section the consequences of the previous findings in terms of remote sensing are  
 15 explored, keeping in mind that only the scattering is taken into account in this paper, and no  
 16 other radar issues. The first obvious one is that a single pulse is not enough to achieve a  
 17 robust measure. Indeed as shown before a single measure basically yields any measured  
 18 intensity over a wide range; and it is impossible to relate it to a given average  $LWC$  or rain  
 19 rate. This is precisely why in practice; an average over typically 100 – 200 pulses over  
 20 approximately 0.1s is used. The underlying assumption is that the successive pulses

1 correspond to independent realisations of the drop positions (drops are moving during this  
2 time interval), meaning that the average value over the pulses yields the desired quantity  
3  $I_{simple}$ , which is free of possible interferences influence.

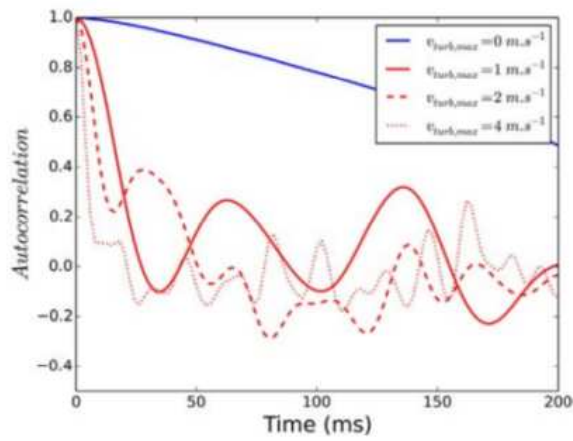
4 In order to study this issue, we use the model presented in section 2, with either a ballistic or a  
5 so called “turbulent” velocity affected to each drop, to represent the temporal evolution over 1  
6 s. Figure 8 (left column) displays the temporal evolution of the backscattered intensity by the  
7 radar in the horizontal polarisation (standard set of parameters is used) for different values of  
8  $v_{trub,max}$ . Computations are carried out each 0.002 s (500 time steps for the simulated second).  
9 Similar curves were found for other realisations. The green long-dash curve corresponds to  
10  $I_{simple,bal}$  and is basically constant during the simulated second. The slight variation noticed on  
11 the curve is simply due to the fact that at each time step some drops are entering the studied  
12 volume from the top and some are leaving from the bottom. Given that it is not exactly the  
13 same ones, this results in slight variations of total water content. Here the slight decrease  
14 means that for this specific realisation, the  $LWC$  was slightly larger at the bottom than at the  
15 top of the generated volume. The curves obtained with the “ballistic” or “turbulent” velocities  
16 are plotted respectively in dash blue and solid red. Figure 8 (right column) displays the same  
17 curves but with an average over 0.1 s (moving window). It appears that the fluctuations  
18 observed at the highest temporal resolution quickly increase with the level of turbulence  
19 inputted in the model (simplistically represented with the help of  $v_{trub,max}$ ). With the 0.1 s  
20 moving window average; the slow fluctuations without turbulence (simply  $v_{bal}$ ) are not  
21 dampened. This can be considered as surprising given that during a 0.1 s interval drops are  
22 moving 5 to 80 cm in this case, which is greater than the radar wave length. It is due to the  
23 fact that the correlations between the drop velocities are too strong. This results in realisations  
24 of drops’ locations that are not independent enough to validate the assumption that successive  
25 pulses yield independent realisations. Same kind of “slow” fluctuations are noted on other  
26 realisations, with usually large deviations (either positive or negative) from the  $I_{simple}$  curve.  
27 When the turbulent velocity  $v_{trub}$  is increased, it appears that fluctuations are much more  
28 pronounced at the highest temporal resolution, and 0.1 s average closer to the  $I_{simple}$  (more  
29 visible for  $v_{trub,max} = 4 \text{ m.s}^{-1}$ ). This is more in agreement with radarist experience. To  
30 investigate further this point, the decorrelation time of the signal was computed for the

1 various values of  $v_{trub,max}$ , similarly to what Capsoni et al. (2001) did. Results are plotted Fig.  
 2 9, and enable to quantify more precisely this effect. If a level of autocorrelation equal to 0.5 is  
 3 taken as a threshold to define the decorrelation time, we find values equal to 200, 16, 9 and 5  
 4 ms for  $v_{trub,max}$  equal to respectively 0, 1, 2 and 4  $m.s^{-1}$ . These values are compatible with  
 5 Capsoni et al. (2001) findings. It means that to properly reproduce backscattering properties  
 6 of the hydrometeors within the fixed volume, one has to take into account turbulent velocity  
 7 of drops. Further investigations taking into account radar technology aspects (antenna and  
 8 beam pattern...) will be needed to confirm this on radar measurement. It is likely that a more  
 9 realistic model of turbulent velocities would yield better results.



10  
 11 Figure 8. (Left column) Temporal evolution of the intensity measured by a radar on the  
 12 horizontal polarisation ( $I_{h,radar}$ ) during 1 s, by modelling drops either with a “ballistic” (dash  
 13 blue) or “turbulent” (solid red) velocity, along  $I_{simple}$  (long dash green). Each line correspond  
 14 to a value of  $v_{trub,max}$  (Right column) Same as in left, with a 0.1 s moving window average.

15



1

2 Figure 9. Autocorrelation of the simulated backscattered signal for various values of  $v_{turb,max}$ .

3

4

5 5) Conclusions

6 In this paper, we developed a 3D rain drop field generator. We used it to numerically mimic  
 7 the scattering produced by hydrometeors contained in a fixed scanned volume of  $50 \times 50 \times 50$   
 8  $m^3$  and its evolution over 1 s. The model is based on Universal Multifractal cascades down to  
 9 0.5 m and a homogeneous distribution of drops below.

10 The primary goal was to investigate the influence of drops' positions, and we show that as  
 11 theoretically expected, we retrieve an exponential distribution for potential measured  
 12 horizontal reflectivity. Given that 0.5 m is much greater than the radar wavelength, we found  
 13 that the clustering of drops has no influence on the results. The model was developed for rain  
 14 drops, and it should be revisited to adapt it to cloud droplets. Indeed they are much smaller  
 15 and therefore more likely to remain correlated to wind turbulence and behave as a passive  
 16 scalar down to scales smaller than 0.5 m and possibly smaller than the radar wavelength.  
 17 Interestingly, a much thinner dispersion of values according to drops' positions is observed on  
 18 differential reflectivity due the correlation between the interferences associated to horizontally  
 19 and vertically polarized waves. Now that the 3D rain drop field generator is available, it  
 20 should be used in future works to develop an actual radar simulator taking into account effects  
 21 such as antenna direction and range weighting functions, or propagation effect between the  
 22 radar and hydrometeors (notably the presence of non clear air), on a more representative  
 23 geometrical setting (not a cubic box). This would enable to actually investigate the influence

1 of drops' positions on the various parameters of the rainfall estimation process with radars.  
2 Other radar quantities, such as the attenuation, the (specific) differential phase and the  
3 standard radar relations linking them to rain rates, should also be addressed in extended  
4 version of this model. A crucial point will also be to study more precisely the role of the DSD,  
5 which has been shown to be one of the most influential inputs of the model, and notably to  
6 relax the coarse assumption of a homogenous DSD over the scanned volume, as argued in this  
7 paper.

8 The analysis of the temporal evolution over 1 s showed that a simple ballistic velocity for  
9 drops did not enable to reproduce radar measurements, and that a "turbulent" velocity should  
10 be introduced. Currently a very simplistic model was implemented and further investigation  
11 should include a coupling with a much more realistic model of wind turbulence, for example  
12 one simulated with multifractal cascades (Schertzer and Tchiguirinskaia, 2015), to reproduce  
13 more accurately radar measurements.

14 Finally, it will be necessary to confront this numerical experiment with dedicated scans of  
15 actual radar measurements. This will be possible with the newly operating X-band radar  
16 installed on the campus of Ecole des Ponts ParisTech where the authors are working.

17

## 18 Acknowledgements

19 The authors thank Alexis Berne for fruitful discussion and suggestions in the framework of  
20 Partenariat Hubert Curien – Germaine de Staël (PROJET N° 32709UK). The authors greatly  
21 acknowledge partial financial support from the Chair "Hydrology for Resilient Cities"  
22 (endowed by Veolia) of Ecole des Ponts ParisTech, and EU NEW-INTERREG IV RainGain  
23 Project ([www.raingain.eu](http://www.raingain.eu)).

24

## 25 References

26 Anagnostou, E.N., Krajewski, W. F., 1997. Simulation of radar reflectivity fields : Algorithm  
27 formulation and evaluation. *Water Resources Research* 33(6), 1419-1428.

28 Battaglia, A., Rustemeier, E., Tokay, A., Blahak, U., Simmer, C., 2010. PARSIVEL Snow  
29 Observations: A Critical Assessment. *Journal of Atmospheric and Oceanic Technology* 27(2),  
30 333-344.

- 1 Beard, K.V., 1977. Terminal velocity adjustment for cloud and precipitation aloft. *J. Atmos.*  
2 *Sci.* 34, 1293-1298.
- 3 Bringi, V. N., Chandrasekar, V., 2001. *Polarimetric Doppler weather radar: principles and*  
4 *applications.* Cambridge University Press, New York, USA.
- 5 Bringi, V.N., Thurai, M., Brunkow, D.A., 2008. Measurements and inferences of raindrop  
6 canting angles. *Electronics Letters* 44(24), 1425-1426.
- 7 Capsoni, C., D'Amico, M., 1998. A physically Based Radar simulation. *Journal of*  
8 *Atmospheric and Oceanic Technology* 15(2), 593-598.
- 9 Capsoni C. , D'Amico, M., Nebuloni, R., 2001. A Multiparameter Polarimetric Radar  
10 Simulator. *Journal of Atmospheric and Oceanic Technology* 18(11), 1799-1809.
- 11 Caumont O. et al., 2006. A Radar Simulator for High-Resolution Nonhydrostatic Models.  
12 *Journal of Atmospheric and Oceanic Technology* 23(8), 1049-1067.
- 13 Cheong, B.L., Palmer, R.D., Xue, M., 2008. A times series weather radar simulator based on  
14 high resolution atmospheric model. *Journal of Atmospheric and Oceanic Technology*  
15 25(2),230-243.
- 16 De Montera, L., Verrier, S., Mallet, C., Barthes, L., 2010. A passive scalar-like model for  
17 rain applicable up to storm scale, *Atm. Res.* 98(1), 140-147.
- 18 Desaulnier-Soucy, N., Lovejoy, S., Schertzer, D., 2001. The continuum limit in rain and the  
19 HYDROP experiment. *J. Atm. Res.* 59-60, 163-197.
- 20 Doviak R. J. and D. S. Zrníc 1993 :*Doppler Radar and weather observations* 2nd ed. academic  
21 Press 562 pp.
- 22 Erkelens, J. S., Venema, V. K. C., Russchenberg, H. W. J., Ligthart, L. P., 2001. Coherent  
23 scattering of microwaves by particles: evidence from clouds and smoke. *J. Atmos. Sci.* 58,  
24 1091–1102, doi: [http://dx.doi.org/10.1175/1520-0469\(2001\)058<1091:CSOMBP>2.0.CO;2](http://dx.doi.org/10.1175/1520-0469(2001)058<1091:CSOMBP>2.0.CO;2).
- 25 Gires, A., Tchiguirinskaia, I., Schertzer, D., Lovejoy, S., 2011. Analyses multifractales et  
26 spatio-temporelles des précipitations du modèle Mésó-NH et des données radar. *Hydrol. Sci.*  
27 *J.* 56(3), 380-396



- 1 Gires, A., Tchiguirinskaia, I., Schertzer, D., Berne A., 2015. 2DVD Data Revisited:  
2 Multifractal Insights into Cuts of the Spatiotemporal Rainfall Process. *Journal of*  
3 *Hydrometeorology* 16(2), 548-562, doi: 10.1175/JHM-D-14-0127.1.
- 4 Jameson, A., Kostinski, B., 2010a. Partially coherent backscatter in radar observations of  
5 precipitation. *J. Atmos. Sci.* 67, 1928–1946, doi: <http://dx.doi.org/10.1175/2010JAS3336.1>.
- 6 Jameson, A., Kostinski, B., 2010b. Direct observations of coherent backscatter of radar waves  
7 in precipitation. *J. Atmos. Sci.* 67, 3000–3005, doi: <http://dx.doi.org/10.1175/2010JAS3488.1>.
- 8 Kawas, M. L., Chen Z., 1989. A radar-based stochastic model for the time-space arrivals of  
9 the rain fields onto a geographical region. *Stochastic Hydrology and Hydraulics* 3(4) , 261-  
10 280.
- 11 Knight, C., Miller, L., 1998. Early radar echoes from small, warm cumulus: bragg and  
12 hydrometeor scattering. *J. Atmos. Sci.* 55, 2974–2992, doi: [http://dx.doi.org/10.1175/1520-  
13 0469\(1998\)055<2974:ERFSW>2.0.CO;2](http://dx.doi.org/10.1175/1520-0469(1998)055<2974:ERFSW>2.0.CO;2).
- 14 Krajewski, W., Raghavan, R., Chandrasekar, V., 1993. Physically based simulation of radar  
15 rainfall radar using a space time rainfall model. *Journal of Applied Meteorology and*  
16 *Climatology* 32 (2), 268-283.
- 17 Kobayashi, S., Oguchi, T., 2007a. Multiple-scattering formulation of pulsed beam waves in  
18 hydrometeors and its application to millimeter-wave weather radar. *IEEE Geosci. Remote*  
19 *Sens. Lett.* 4, 13-17.
- 20 Kobayashi, S., Ito, S., Tanelli, S., Oguchi, T., Im, E., 2007b. A time-dependent multiple  
21 scattering theory for a pulsed radar with a finite beamwidth. *Radio Sci.* 42, RS4001,  
22 doi:10.1029/2006RS003555.
- 23 Kobayashi, S., Tanelli S., Im E., 2005. Second-order multiple scattering theory associated  
24 with backscattering enhancement for a millimeter wavelength weather radar with a finite  
25 beam width. *Radio Sci.* 40, RS6015, doi:10.1029/2004RS003219.
- 26 Kobayashi, S., Oguchi, T., Tanelli, S., Im, E., 2007. Backscattering enhancement on spheroid-  
27 shaped hydrometeors: Considerations in water and ice particles of uniform size and Marshall-  
28 Palmer distributed rains. *Radio Sci.* 42, RS2001, doi:10.1029/2006RS003503.
- 29 Lawson, J. L., Uhlenbeck, G. E., 1950. *Threshold Signals*. McGraw-Hill, New York, USA.

- 1 Leinonen, J., 2014. High-level interface to T-matrix scattering calculations: architecture,  
2 capabilities and limitations. *Optics Express* 22(2), 1655-1660.
- 3 Leinonen, J., Moisseev, D., Leskinen, M., Petersen, W.A., 2012. A Climatology of  
4 Disdrometer Measurements of Rainfall in Finland over Five Years with Implications for  
5 Global Radar Observations. *Journal of Applied Meteorology and Climatology* 51(2), 392-404.
- 6 Lhermitte, R., 1988. Cloud and precipitation sensing at 94 GHz. *IEEE Trans. Geosci. Remote*  
7 *Sens.* 26, 207–216.
- 8 Lilley, M., Lovejoy, S., Desaulniers-Soucy, N., Schertzer, D., 2006. Multifractal large number  
9 of drops limit in rain. *J. Hydrol.* 328(1-2), 20-37, 2006.
- 10 Liu, X.C., Gao, T.C., Liu, L., 2014. A video precipitation sensor for imaging and velocimetry  
11 of hydrometeors. *Atmos. Meas. Tech.* 7(7), 2037-2046, [www.atmos-meas-](http://www.atmos-meas-tech.net/7/2037/2014/)  
12 [tech.net/7/2037/2014/](http://www.atmos-meas-tech.net/7/2037/2014/) doi:10.5194/amt-7-2037-2014
- 13 Lovejoy, S., Schertzer, D., 1990. Multifractals, universality classes, satellite and radar  
14 measurements of clouds and rain. *J. Geophys. Res.* 95, 2021-2034.
- 15 Lovejoy, S., Duncan, M.R., Schertzer, D., 1996. Scalar Multifractal Radar Observers  
16 Problem. *J. Geophys. Res.* 101, 26479-92.
- 17 Merker, C., Peters, G., Clemens, M., Lengfeld, K., Ament, F., 2015. A novel approach for  
18 absolute radar calibration: formulation and theoretical validation. *Atmos. Meas. Tech.* 8,  
19 2521-2530, doi:10.5194/amt-8-2521-2015.
- 20 Mishchenko, M.I., Travis, L.D., Mackowski, D.W., 1996. T-matrix computations of light  
21 scattering by nonspherical particles: A review. *Journal of Quantitative Spectroscopy and*  
22 *Radiative Transfer* 55(5), 535-575.
- 23 Montero-Martinez, G., Kostinski, A., Shaw, R., Garcia-Garcia, F., 2009. Do all raindrops fall  
24 at terminal speed? *Geophysical Research Letters* 36, L11818, doi:10.1029/2008GL037111.
- 25 Niu, S., Jia, X., Sang, J., Lu, C., Liu, Y., 2010. Distributions of Raindrop Sizes and Fall  
26 Velocities in a Semiarid Plateau Climate: Convective versus Stratiform Rains. *Journal of*  
27 *Applied Meteorology and Climatology* 49(4), 632-645, doi: 10.1175/2009JAMC2208.1
- 28 Oguchi, T., 1977. Scattering properties of Pruppacher-and-Pitter form raindrops and cross  
29 polarization due to rain: Calculations at 11, 13, 19.3, and 34.8 GHz. *Radio Sci.* 12, 41-51.

1 Okamura, S., Oguchi, T., 2010. Electromagnetic wave propagation in rain and polarization  
2 effects. *Proceedings of the Japan Academy. Series B, Physical and Biological Sciences* 86(6),  
3 539-562, <http://doi.org/10.2183/pjab.86.539>

4 Sachinanda, M., Zrnica, D.S. 1987. Rain Rate Estimates from Differential Polarization  
5 Measurements. *Journal of Atmospheric and Oceanic Technology*, 4(4), 588-598.

6 Schertzer, D., Lovejoy, S., 2011. Multifractals, generalized scale invariance and complexity  
7 in geophysics. *International Journal of Bifurcation and Chaos* 21(12), 3417-3456.

8 Schertzer, D., Tchiguirinskaia, I., Lovejoy, S., 2012. Getting Higher Resolution Rainfall  
9 Estimates: X-Band Radar Technology and Multifractal Drop Distribution. *Proceedings of the*  
10 *Weather Radar and Hydrology Symposium Held in Exeter, UK, April 2011, IAHS Publ.* 351.

11 Schertzer, D., Tchiguirinskaia, I., 2015. Multifractal vector fields and stochastic Clifford  
12 algebra, *Chaos*, 25, 123127(1-17), doi: 10.1063/1.4937364.

13 Schleiss, M., Smith, J., 2015. A Method to Estimate the 3D-Time Structure of the Raindrop  
14 Size Distribution Using Radar and Disdrometer Data. *J. Hydrometeorol.* 16, 1222–1242.

15 Schmitt, F., Schertzer, D. L., Lovejoy, S., Brunet, G., 1996. Multifractal temperature and flux  
16 of temperature variance in fully developed turbulence. *Europhys. Lett.*, 34(3), 195-200.

17 Steiner, M., 2005. Estimation of Precipitation Using Ground-based, Active Microwave  
18 Sensors. In *Encyclopedia of hydrological sciences*, Anderson M.G. (ed), Wiley.

19 Tchiguirinskaia, I., D. Schertzer, C. T. Hoang and S. Lovejoy, 2012: Multifractal study of  
20 three storms with different dynamics over the Paris region. *Weather Radar and Hydrology*. R.  
21 Moore, S.J. Cole and A.J. Illingworth Eds. IAHS Press Wallingford U.K., 421-426

22 Thurai, M., Bringi, V.N., 2005. Drop axis ratios from 2D video disdrometer. *J. Atmos. Ocean.*  
23 *Technol.* 22(7), 966-978.

24 Thurai, M., Szakáll, M., Bringi, V.N., Beard, K.V., Mitra, S.K., Borrmann, S., 2009. Drop  
25 shapes and axis ratio distributions: Comparison between 2D video disdrometer and wind-  
26 tunnel measurements. *Journal of Atmospheric and Oceanic Technology* 26(7), 1427-1432.

27 Thurai, M., Bringi, V.N., Petersen, W.A., 2009. Rain microstructure retrievals using 2-D  
28 video disdrometer and C-band polarimetric radar. *Adv. Geosci.* 20, 13-18.

1 Thurai, M., Bringi, V.N., Petersen, W.A., Gatlin, P.N., 2013. Drop Shapes and Fall Speeds in  
2 Rain: Two Contrasting Examples. *Journal of Applied Meteorology and Climatology* 52(11),  
3 2567-2581, doi: <http://dx.doi.org/10.1175/JAMC-D-12-085.1>

4 Verrier, S., Mallet, C., Barthès, L., 2011. Multiscaling properties of rain in the time domain,  
5 taking into account rain support biases . *Journal of Geophysical Research: Atmospheres*,  
6 116(D20), D20119, <http://dx.doi.org/10.1029/2011JD015719>

7 Verrier, S., De Montera, L., Barthès, L., Mallet, C. , 2010. Multifractal analysis of African  
8 monsoon rain fields, taking into account the zero rain-rate problem . *Journal of Hydrology*  
9 389 (1-2), 111-120.

10

11